2.5D Deep Learning Inversion of LWD and Deep-Sensing EM Measurements Across Formations with Dipping Faults

Kyubo Noh, David Pardo, and Carlos Torres-Verdín, *Member, IEEE*

***Abstract*—Deep learning (DL) inversion of induction logging measurements is used in well geosteering for real-time imaging of the distribution of subsurface electrical conductivity. We develop a DL inversion workflow to solve 2.5-dimensional (2.5D) inverse problems arising in well geosteering. The inversion workflow employs three DL modules: a "look-around" fault detection module and two inversion modules for reconstructing anisotropic resistivity models in the presence or absence of fault planes, respectively. Our DL approach is capable of detecting and quantifying arbitrary dipping fault planes in real-time. We compare inversion performance considering only short logging-while-drilling (LWD) measurements vs. using both short LWD and deep-sensing measurements. The latter measurements provide enhanced depth-of-investigation while minimizing uncertainty. We also obtain improved results when using multi-dimensional inversion, especially nearby fault planes. This study verifies the applicability of real-time 2.5D DL inversion across arbitrary faulted formations for well geosteering.**

***Index Terms*— Deep learning, fault detection, geosteering, induction logging, inverse problem**

I. Introduction

WELL geosteering is used for the real-time control of underground well trajectories, and it is one of the most critical techniques to maximize the contact of drilled wells within the target geological units [1], [2]. Borehole electromagnetic (EM) induction measurements contain information about the surrounding rocks and saturating fluids [3] and are often employed for well geosteering purposes. This requires interpretation of borehole induction measurements via an inversion method.

One-point-five-dimensional (1.5D) inversion has been widely implemented for well geosteering (see, e.g., [4], [5]) because of its low computational cost. However, it may cause critical misinterpretations in certain geological structures: for example, when the well trajectory crosses a geological fault. In such cases, a multi-dimensional inversion method has a higher capacity of imaging the true resistivity structure [6], [7]. However, multi-dimensional inversion is often computationally expensive due to the need of performing CPU-time consuming forward simulations. To achieve multi-dimensional inversion of induction logging measurements in almost real-time, some authors have proposed multiple fast forward simulation methods (see, e.g., [7]– [9]). Despite these efforts, there is still a need for faster and more reliable multi-dimensional inversion methods to achieve the true meaning of real-time imaging.

Meanwhile, modern machine learning methods such as deep learning (DL) are now widely employed for solving various scientific and engineering problems [10]–[12]. In particular, DL methods have recently been applied to solve geophysical inverse problems [13], [14]. DL inversion offers the practical possibility of real-time imaging of spatially complex subsurface structures. Motivated by this real-time inversion alternative, a few pioneering studies applied DL inversion of borehole induction measurements mostly assuming a piecewise 1.5-D subsurface structure [15]–[18]. An extension to two-point-five-dimensional (2.5D) geometries was proposed in [19], although this study was restricted to short-spaced LWD measurements and vertical faults. This paper extends the 2.5D DL inversion method proposed in [19] to the case of deep-sensing measurements and incorporates fault geometries of varying dip angles. Thus, we invert simultaneously both short LWD and deep-sensing measurements to infer the spatial distribution of electrical conductivity around the well trajectory.

The letter is organized as follows: In section II, we describe the DL inversion method, including our multi-dimensional inversion workflow composed of three modules. We also compare training results obtained with and without utilizing deep-sensing measurements. Section III considers a synthetic complex model containing a graben structure with two dipping faults and compares DL inversion results with and without using deep-sensing measurements. Conclusions follow in section IV.

II. Method

A. Inversion workflow

Our inversion workflow consists of a fault prediction module and two inversion modules to predict the resistivity structure

This work reported in this paper was supported by the University of Texas at Austin's Research Consortium on Formation Evaluation, jointly sponsored by Aramco, Baker Hughes, BHP Billiton, BP, Chevron, CNOOC International, ConocoPhillips, ENI, Equinor ASA, ExxonMobil, INPEX, Lundin-Norway, Occidental, Oil Search Alaska, Petrobras, Repsol, Schlumberger, Shell, Total, Wintershall-DEA, and Woodside Petroleum Limited. The authors also acknowledge the Texas Advanced Computing Center (TACC) at the University of Texas at Austin for providing HPC resources that have contributed to the research results reported in this paper. URL: http://www.tacc.utexas.edu

K. Noh and C. Torres-Verdín are with The University of Texas at Austin, Austin, TX 78712 (email: kyubonoh@gmail.com, cverdin@austin.texas.edu). D. Pardo is with University of the Basque Country, Leioa, Spain; Basque Center for Applied Mathematics, Bilbao, Spain; and Ikerbasque, Bilbao, Spain. (email: dzubiaur@gmail.com)

.

with or without fault planes, respectively. First, EM logging measurements are segmented with a predefined dimension and input to the prediction module. Then, the prediction module determines the presence or absence of fault planes in the "look-around" dichotomic sense. The local resistivity models are subsequently reconstructed using the corresponding inversion modules based on the fault detection results. The final resistivity model is obtained by stacking and "stitching" together the local resistivity models.

B. Subsurface and trajectory parameterization

We consider two-dimensional earth models composed of three layers. Fig. 1 shows two of these models: one without a geological fault, and another one with it. The first case in Fig. 1a is parameterized with 10 variables ($\boldsymbol{m} \in \mathbb{R}^{10}$, where $\boldsymbol{m}$ is a set of model parameters): six resistivity values, representing horizontal and vertical resistivities of three layers; two dipping angles of bed boundaries; and two vertical distances from the bed boundaries to the logging instrument at the horizontal center of the local trajectory. The second earth model in Fig. 1b contains a dipping fault plane and it is parameterized with 22 variables ($\boldsymbol{m} \in \mathbb{R}^{22}$). Table 1 summarizes the choices of specific values for model and trajectory parameters.

C. Measurements

We consider two types of tri-axial instruments: (a) a short-spaced LWD instrument with ten transmitters (Txs) operating at 2 MHz and two receivers (Rxs), with minimum and maximum Tx-Rx offsets of approximately 0.3 and 1.12 m, respectively; and (b) a tri-axial deep-sensing instrument with one Tx operating at 10 kHz and one Rx spaced 12 m away from the Tx. The latter logging instrument has a larger depth-of-investigation (DOI) than the LWD instrument because of the larger Tx-Rx offset and lower operating frequency. We consider both attenuation and phase components of one co-axial, two co-planar, and one cross-coupling, the so called Geosignal component. We refer to the Appendix in [16] for the corresponding postprocessing and [19] for the importance of selecting multiple components, especially the cross-coupling component, as an input for the multi-dimensional inversion.

D. Training and test data sets

We generate two independent datasets: one for the case without fault, and one for the case with a fault. For each of them, we simulate 20K samples consisting of trajectory, resistivity model, and their corresponding 2.5D forward responses calculated using a high-order mesh-adaptive simulator [20]. To enhance the robustness of DL inversion against measurement noise, we follow [21] and take their proposed "augmented measurement noise" strategy of triplicating the original data sets by contaminating them with zero-mean Gaussian noise with maximum intensities of 0.1 dB and 0.4 degrees for the short LWD measurements and 0.004 dB and 0.4 degrees for the deep-sensing measurements. Each data set then includes 60K samples. We employ 85% of those samples for training, and the remaining 15% for testing.

E. Deep learning training process

We first train for a binary classification problem to determine the possible presence or not of a geological fault. For that, we build an objective function using cross-entropy with a sigmoid function.

We also train for the two independent modules to determine the earth models. We follow [16] and simultaneously train the forward and inverse operators instead of training only the inverse operator. The approach is realized by minimizing the following problem:

$$\left(F_{\phi^*}, I_{\theta^*}\right) := \arg\min_{\phi\in\Phi,\theta\in\Theta} \begin{Bmatrix} \left\| \left(F_\phi \circ I_\theta\right)(\boldsymbol{M},\boldsymbol{T}) - \boldsymbol{M} \right\|_2^2 \\ + \left\| F_\phi(\boldsymbol{P},\boldsymbol{T}) - \boldsymbol{M} \right\|_2^2 \end{Bmatrix}, \quad (1)$$

where **P**, **M**, **T** denote subsurface properties, measurements, and well trajectory, respectively, and F_ϕ and I_θ are DL architectures approximating forward and inverse functions that contain unknown weights ϕ and θ, respectively. The first term in the right-hand-side of Eq. (1) is designed to guarantee that I_θ is the inverse operator of F_ϕ, while the second term ensures that the forward operator F is properly approximated by F_ϕ.

We select a deep residual neural network (ResNet) [22] with 1D convolutional layers to construct the forward, inverse, and classification modules with properly varying input and output shapes. In addition, we add non-trainable Gaussian noisy layers to enhance robustness against measurement noise [21]. By using TensorFlow [23] and Keras [24], we independently carry out the training process of classification and inversion modules for the two types of input measurements: short LWD and both short LWD and deep-sensing measurements. Each training process takes approximately 6 CPU hours using an Nvidia GTX machine equipped with Intel Xeon E5-2620 v4 CPU and four Nvidia 1080-TI GPUs.

F. Training results

Table 2 compares the accuracy of the binary classification over the testing data set when using only short LWD measurements vs. both short LWD and deep-sensing measurements. When using only short LWD measurements, prediction accuracies are approximately 99.67 and 98.67 percent for the models without and with fault planes, respectively. When adding deep-sensing measurements, the results slightly increase to 99.70 and 98.74 percent. The classification module indicating the possible presence of a nearby fault shows high accuracy independently of the use of deep-sensing measurements.

Table 3 summarizes the root-mean-squared error (RMSE) of the earth model parameters over the test data sets. Regardless of the fault presence in the model, results show higher accuracy about the host layer resistivities than about the neighboring layers resistivities. Horizontal resistivity shows higher accuracy than vertical resistivity in both hosting and neighboring layers. When deep-sensing measurements are used together with short LWD measurements, estimation of resistivities of neighboring layers, distances, and angles of layer interfaces improve, while the accuracy of the host layer resistivities stays at the same level. These results are consistent with the underlying physics

concerning directional sensitivity and DOI associated with different input components and types of logging instruments.

Comparison of the results obtained for the faulted models show slightly higher RMSE—7 to 35 percent—than those without fault planes because faulted models involve a larger number of unknowns. When adding deep-sensing measurements, we observe a similar level of accuracy in terms of the horizontal location, but the accuracy of the dip angle dramatically improves.

In summary, LWD measurements are sufficient to determine specific parameters such as hosting resistivities, fault presence, and horizontal location of fault planes. However, the use of deep-sensing measurements significantly enhances the inversion results concerning multi-dimensional features, e.g., information on neighboring layers, and fault dipping angle.

III. Numerical Application

We now consider a three-dimensional (3D) geological model. Fig. 2 shows a cross-section of the 3D model at the center of the *y*-axis and the 3D trajectory projected on the cross-section. The model contains two opposite dipping normal faults (with -30 and 30 degrees of dip angle, respectively) leading to the subsidence of a graben. We use the open-source code GemPy [25] to generate the 3D geological model with a half-meter grid size. We then extract two-dimensional planes along the trajectory and interpolate them into a finer centimeter scale for 2.5D simulations. Figure 3a shows the corresponding horizontal and vertical resistivities of the three-layered model. We then carry out 2.5D forward modeling using a finite element method. The simulated measurements are contaminated with a noise level similar to that of the training data set.

Figs. 3b and 3c show the DL inversion results obtained by using only short LWD measurements and both short LWD and deep-sensing measurements, respectively. Both results agree in terms of the hosting layer resistivities. Fig. 4 shows the reconstructed short LWD measurements obtained when using the inversion results of Figs. 3b and 3c. We observe accurate prediction of the short LWD measurements thanks to good reconstructions of hosting resistivities. The overall RMSEs are nearby [0.149 dB, 0.424 degrees], when inverting short LWD measurements only, and [0.121 dB, 0.401 degrees], when inverting both short LWD and deep-sensing measurements, which are comparable with added noise level. Besides the well reconstruction of hosting resistivities, multi-dimensional features such as structure of adjacent layers and fault planes differ each other in Figs. 3b and 3c. When using only short LWD measurements, inversion results in Fig. 3b show good agreement concerning close layer interfaces at a few locations (for example, across horizontal position ranges [0, 10], [20, 30], and [120, 140]). In other areas, predictions poorly reconstruct layer interfaces and neighboring resistivities. These predictions improve when adding deep-sensing measurements: in particular, in the reconstruction of neighboring layers and fault-plane dip angles.

Empowered by the low computational cost of DL inversion, we evaluate the uncertainty of the deterministic DL inversion result by simple performing repetitive calculations. First, we reproduce sets of input measurements by multiple times and contaminate each reproduced sample with varying measurement noise. For the following results, we use 100 times for the size of the reproductions. The computation time is about 4 CPU seconds for each measurement point spaced 10 centimeter using a laptop equipped with an Intel i7-7700HQ processor and an Nvidia GeForce GTX 1050 GPU. By applying the inversion workflow and comparing the results obtained from each reproduced measurement, we collect the distributions of inverse solutions. Then the uncertainty from the distributions provides a comprehensive measure of the noise effect, and training accuracy of the DL modules.

To analyze uncertainty results, we focus on the point-by-point standard deviation of the inverted distance to the upper boundary. Fig. 5 compares the results obtained from short LWD measurements only vs. those from both short LWD and deep-sensing measurements. We observe lower deviation values when both types of measurements are input to the inversion. Fig. 6 compares the normalized standard deviations for varying model parameters across the entire well trajectory. The horizontal locations of fault crossings show low standard deviation regardless of the use of deep-sensing measurements. Other features related to the multi-dimensional structure (e.g., dip of fault planes) show the largest decrement of approximately 40 percent when considering deep-sensing measurements. Horizontal resistivities show lower deviation than vertical resistivities.

IV. Conclusion

We developed a DL inversion workflow that images the 2.5D resistivity structure of potentially fractured subsurface structures from EM borehole induction measurements for real-time well geosteering applications. The workflow consists of one classification module and two inversion modules—to consider the cases without and with fault planes, respectively. Using the DL inversion workflow, we investigated the benefits of incorporating deep-sensing measurements in the inversion results. Two types of input measurements were considered—one consisting of only LWD measurements and another employing both LWD and deep-sensing measurements. We showed via synthetic examples that: (1) it is possible to detect and reconstruct fault planes and hosting resistivities from LWD measurements, and (2) the performance of multi-dimensional inversion significantly improves by employing also deep-sensing measurements. In addition, we were able to produce uncertainty results thanks to the fast evaluation of the DL inversion method. These results are useful for interpretation and decision-making in real field applications.

The developed workflow assumes that the subsurface resistivity structure is a continuum of local three-layer structures possibly crossed by non-perpendicular and non-azimuthal fault planes. Future research will focus on the extension of the workflow toward full 3D inversion with more flexibility in model assumptions.

References

[1] W. G. Lesso and S. v. Kashikar, "Principles and procedures of geosteering," in *Proceedings of the Drilling Conference*, 1996. doi: 10.2118/35051-ms.

[2] S. Alyaev, E. Suter, R. B. Bratvold, A. Hong, X. Luo, and K. Fossum, "A decision support system for multi-target geosteering," *Journal of Petroleum Science and Engineering*, vol. 183, 2019, doi: 10.1016/j.petrol.2019.106381.

[3] D. Pardo, P. J. Matuszyk, V. Puzyrev, C. Torres-Verdín, M. J. Nam, and V. M. Calo, "Chapter 3 - Modeling of resistivity geophysical measurements," in *Modeling of Resistivity and Acoustic Borehole Logging Measurements Using Finite Element Methods*, Elsevier, 2021, pp. 77–113. doi: 10.1016/B978-0-12-821454-1.00009-1.

[4] X. Hu, Y. Fan, S. Deng, X. Yuan, and H. Li, "Electromagnetic Logging Response in Multilayered Formation with Arbitrary Uniaxially Electrical Anisotropy," *IEEE Transactions on Geoscience and Remote Sensing*, vol. 58, no. 3, 2020, doi: 10.1109/TGRS.2019.2952952.

[5] D. Pardo and C. Torres-Verdín, "Fast 1D inversion of logging-while-drilling resistivity measurements for improved estimation of formation resistivity in high-angle and horizontal wells," *Geophysics*, vol. 80, no. 2, 2015, doi: 10.1190/GEO2014-0211.1.

[6] Z. Wu, Y. Fan, J. Wang, R. Zhang, and Q. H. Liu, "Application of 2.5-D Finite Difference Method in Logging-While-Drilling Electromagnetic Measurements for Complex Scenarios," *IEEE Geoscience and Remote Sensing Letters*, vol. 17, no. 4, 2020, doi: 10.1109/LGRS.2019.2926740.

[7] V. Puzyrev, D. Pardo, V. Calo, and C. Torres-Verdín, "Recent advances on the inversion of deep directional borehole resistivity measurements," *ASEG Extended Abstracts*, vol. 2019, no. 1, 2019, doi: 10.1080/22020586.2019.12073031.

[8] M. Thiel, M. Bower, and D. Omeragic, "2D reservoir imaging using deep directional resistivity measurements," *Petrophysics*, vol. 59, no. 2, 2018, doi: 10.30632/PJV59N2-2018a7.

[9] D. Marchant, N. Clegg, L. Rawsthorne, and J. Kunnas, "3D inversion of electromagnetic logging-while-drilling data," *ASEG Extended Abstracts*, 2019, doi: 10.1080/22020586.2019.12073097.

[10] J. Schmidhuber, "Deep Learning in neural networks: An overview," *Neural Networks*, vol. 61. 2015. doi: 10.1016/j.neunet.2014.09.003.

[11] Y. Bengio, "Learning deep architectures for AI," *Foundations and Trends in Machine Learning*, vol. 2, no. 1, 2009, doi: 10.1561/2200000006.

[12] Y. Lecun, Y. Bengio, and G. Hinton, "Deep learning," *Nature*, vol. 521, no. 7553. 2015. doi: 10.1038/nature14539.

[13] M. Araya-Polo, J. Jennings, A. Adler, and T. Dahlke, "Deep-learning tomography," *Leading Edge*, vol. 37, no. 1, 2018, doi: 10.1190/tle37010058.1.

[14] D. Colombo, E. Turkoglu, W. Li, E. Sandoval-Curiel, and D. Rovetta, "Physics-driven deep-learning inversion with application to transient electromagnetics," *GEOPHYSICS*, vol. 86, no. 3, 2021, doi: 10.1190/geo2020-0760.1.

[15] Y. Jin, X. Wu, J. Chen, and Y. Huang, "Using a physics-driven deep neural network to solve inverse problems for LWD azimuthal resistivity measurements," *SPWLA 60th Annual Logging Symposium*, 2019. doi: 10.30632/T60ALS-2019_IIII.

[16] M. Shahriari, D. Pardo, J. Rivera, C. Torres-Verdín, A. Picon, J. Del Ser, S. Ossandón, and V. Calo, "Error control and loss functions for the deep learning inversion of borehole resistivity measurements," *International Journal for Numerical Methods in Engineering*, vol. 122, no. 6, 2021, doi: 10.1002/nme.6593.

[17] G. Zhu, M. Gao, F. Kong, and K. Li, "A Fast Inversion of Induction Logging Data in Anisotropic Formation Based on Deep Learning," *IEEE Geoscience and Remote Sensing Letters*, vol. 17, no. 12, 2020, doi: 10.1109/LGRS.2019.2961374.

[18] Y. Hu, R. Guo, Y. Jin, X. Wu, M. Li, A. Abubakar, and J. Chen, "A Supervised Descent Learning Technique for Solving Directional Electromagnetic Logging-While-Drilling Inverse Problems," *IEEE Transactions on Geoscience and Remote Sensing*, vol. 58, no. 11, 2020, doi: 10.1109/TGRS.2020.2986000.

[19] K. Noh, C. Torres-Verdín, and D. Pardo, "Real-Time 2.5D Inversion of LWD Resistivity Measurements Using Deep Learning for Geosteering Applications Across Faulted Formations," *SPWLA 62nd Annual Logging Symposium*, 2021. doi: 10.30632/SPWLA-2021-0104.

[20] Á. Rodríguez-Rozas, D. Pardo, and C. Torres-Verdín, "Fast 2.5D finite element simulations of borehole resistivity measurements," *Computational Geosciences*, vol. 22, no. 5, 2018, doi: 10.1007/s10596-018-9751-7.

[21] K. Noh, D. Pardo, and C. Torres-Verdín, "A Deep Learning Inversion for Noisy Logging-While-Drilling Resistivity Data," *IEEE Transactions on Geoscience and Remote Sensing*, 2021 (Submitted).

[22] K. He, X. Zhang, S. Ren, and J. Sun, "Deep residual learning for image recognition," in *Proceedings of the IEEE Computer Society Conference on Computer Vision and Pattern Recognition*, 2016, doi: 10.1109/CVPR.2016.90.

[23] Abadi, M., et al., "TensorFlow: Large-scale machine learning on heterogeneous systems," tensorflow.org, doi: 10.1190/tle37010058.1.

[24] Chollet, F., "Keras," 2015, https://github.com/fchollet/keras

[25] M. de La Varga, A. Schaaf, and F. Wellmann, "GemPy 1.0: Open-source stochastic geological modeling and inversion," *Geoscientific Model Development*, vol. 12, no. 1, 2019, doi: 10.5194/gmd-12-1-2019.

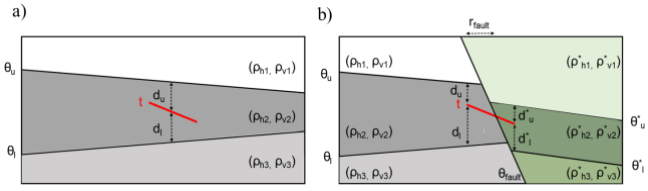

Figure 1. Graphical representations of the spatial resistivity distributions used to describe specific geological conditions in this work. The red line is the local well trajectory. (a) Three-layer model without a crossing fault between a fault plane and the trajectory. (b) Two three-layer models with a fault plane within the local well trajectory.

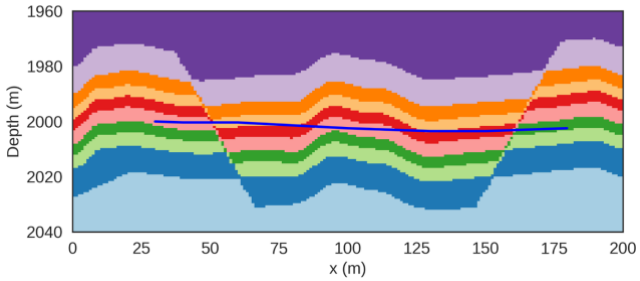

Figure 2. Cross-section of a three-dimensional (3D) geological model representing a graben fault condition. The blue line describes the 3D trajectory projected in *x-depth* space.

Resistivities (ρ_h, ρ_v) (Ohm-m)	Anisotropic factor (ρ_v/ρ_h)	Distance to layers (m)	Dip of layers (°)	Dip of fault (°)	Dip of trajectory (°)	Deviation of trajectory (°/m)
[0.1, 100.0]	[1.0, 10.0]	[0.0, 3.0]	[70.0, 110.0]	[-30, 30]	[83, 97]	[-0.15, 0.15]

Table 1. Ranges of model and well trajectory parameters used to generate the training and test data sets.

Prediction / True	LWD		LWD + Deep Sensing	
	w/oFault	wFault	w/oFault	wFault
w/oFault	8970	30	8973	27
wFault	120	8880	113	8887

Table 2. Results obtained with our classification module trained and tested with noise-contaminated data sets.

Resistivity Model	Input Measurements	ρ_{h_host}	ρ_{v_host}	ρ_{h_neigh}	ρ_{v_neigh}	D_{bed}	Θ_{bed}	D_{fault}	Θ_{fault}
w/oFault	LWD	0.086	0.113	0.344	0.357	0.560	10.545	-	-
w/oFault	LWD+Deep	0.088	0.110	0.187	0.210	0.206	6.328	-	-
wFault	LWD	0.110	0.128	0.352	0.396	0.660	11.264	0.110	12.443
wFault	LWD+Deep	0.107	0.119	0.201	0.251	0.315	8.278	0.104	5.103

Table 3. Root-mean-squared error of test data sets with varying conditions for resistivity models and input measurements. Results obtained for parameters with analogous physical meaning are grouped. Units for resistivities, distances, and angles are $\log_{10}$(Ohm-m), meters, and degrees, respectively. "LWD" and "Deep" for input measurements stand for short LWD and deep-sensing measurements, respectively.

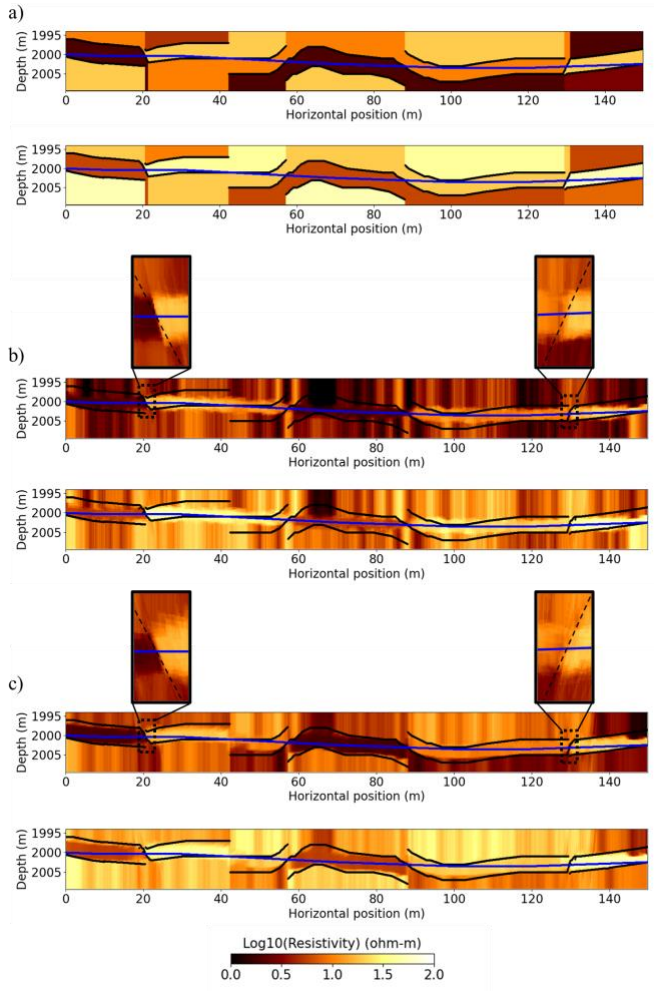

Figure 3. (a) 2.5D three-layered resistivities along the well trajectory shown in Fig. 2. Inverted resistivity models obtained from (b) only LWD measurements and from (c) both LWD and deep-sensing measurements. Upper and lower panels show inverted horizontal and vertical resistivities, respectively. Corresponding well trajectory and adjacent bed boundaries are shown in blue and black solid lines, respectively. Inversion results of faulted segments are zoomed-in with the true geometry of the fault planes marked with black dashed lines for horizontal resistivity models.

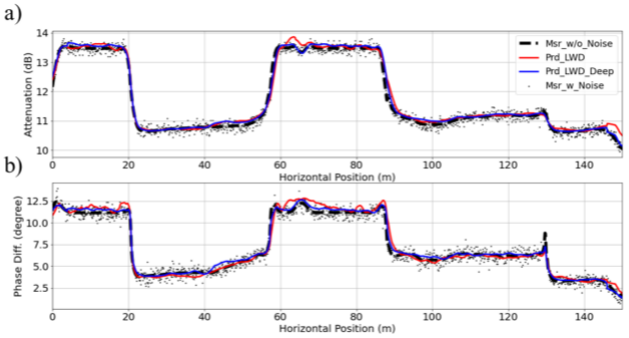

Figure 4. Comparison of noise-free measurements (black dashed lines), noise-contaminated measurements (black dots), and predicted measurements obtained with DL inversion after using only LWD (red solid lines) and both LWD and deep-sensing (blue solid lines) measurements. Upper and lower panels show attenuation and phase difference, respectively, corresponding to the co-axial configuration of the LWD instrument with the longest offset.

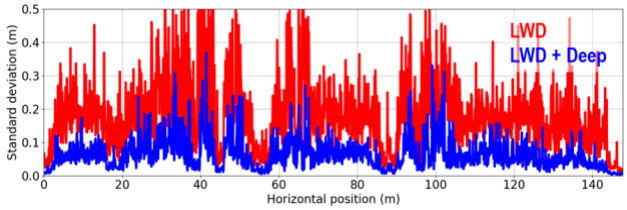

Figure 5. Standard deviation of inverted upper bed boundary positions when using short LWD measurements only (red line) and both short LWD and deep-sensing measurements (blue line).

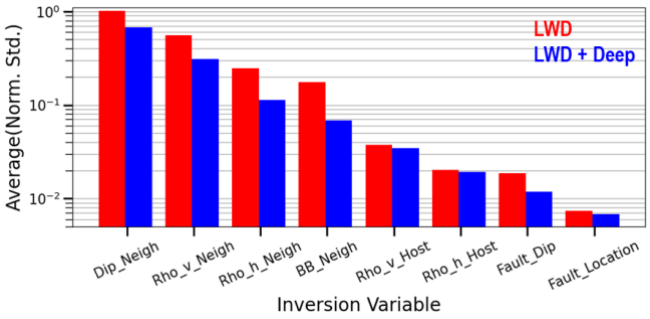

Figure 6. Normalized standard deviation of inversion variables obtained with deep learning inversion modules trained with only short LWD (red bars) and both short LWD and deep-sensing (blue bars) measurements.